ELSEVIER

Contents lists available at ScienceDirect

## Journal of Nuclear Materials

journal homepage: www.elsevier.com/locate/jnucmat



# High-throughput ion irradiation of additively manufactured compositionally complex alloys



Michael Moorehead a,\*, Phalgun Nelaturu a, Mohamed Elbakhshwan a, Calvin Parkin a, Chuan Zhang C, Kumar Sridharan a,b, Dan J. Thoma a,b,d, Adrien Couet a,b

- <sup>a</sup> University of Wisconsin-Madison, Engineering Physics Dept., Madison, WI 53706 USA
- <sup>b</sup> University of Wisconsin-Madison, Materials Science and Engineering Dept., Madison, WI 53706 USA
- <sup>c</sup> Computherm LLC, Middleton, WI 53562 USA
- <sup>d</sup> Grainger Institute for Engineering, Madison, WI 53706 USA

#### ARTICLE INFO

#### Article history: Received 31 August 2020 Revised 30 November 2020 Accepted 3 January 2021 Available online 7 January 2021

Keywords: Additive manufacturing Ion irradiation High throughput High-entropy alloys CALPHAD

## ABSTRACT

Several advanced nuclear reactor designs promise efficiency and safety improvements over the current reactor fleet but are limited by the current set of ASME code-qualified materials. Novel alloys including high-entropy alloys (HEAs), and more broadly compositionally complex alloys (CCAs), have shown promising irradiation-tolerance. However, the vast range of alloy compositions adds to an already timeconsuming alloy development process. In this study, to accelerate the development of novel alloys for nuclear applications, a high-throughput (HTP) methodology has been employed. Additive manufacturing has been used to produce a compositional array of unary, binary, ternary, and quaternary alloys, including several CCAs, which span the Cr-Fe-Mn-Ni composition space. The compositional array was homogenized at 1000°C for 24 hours and each sample was irradiated using 4-MeV Ni<sup>2+</sup> ions at room temperature to a peak damage of 50 dpa, as estimated using SRIM, at the University of Wisconsin Ion Beam Laboratory. A custom XY stage was built to accommodate the large compositional array and half of each sample was masked during irradiation enabling both the irradiated and unirradiated properties of each alloy to be characterized side-by-side. Each alloy was characterized using X-ray fluorescence (XRF), X-ray diffraction (XRD), scanning electron microscopy (SEM), energy dispersive spectroscopy (EDS), and nanoindentation. CALPHAD simulations spanning the entire Cr-Fe-Mn-Ni composition space at 1000°C were performed to compare predicted equilibrium phases with phases identified experimentally from the unirradiated regions of each alloy. Nanoindentation measurements indicate radiation-induced hardening ranging from ~1-1.5 GPa in each of Cr-Fe-Mn-Ni CCAs, which is relatively insensitive to modest changes in alloy composition and comparable to hardening observed in neutron irradiated Cr-Fe-Mn-Ni CCAs in the literature. Overall, a substantial time savings was realized by employing HTP synthesis, irradiation, and characterization in this study compared to conventional techniques, the implications of which are discussed.

© 2021 Elsevier B.V. All rights reserved.

## 1. Introduction and motivation

The development of next-generation nuclear reactors, with improved efficiencies, higher fuel burnups, and enhanced passive safety features will require structural materials with properties beyond those of the currently code-qualified materials [1]. For example, the proposed Traveling Wave Reactor (TWR) requires cladding materials, which can maintain their structural integrity up to a lifetime irradiation damage of ~600 dpa with a peak inner cladding temperature of 650°C [2], while the maximum dose for which me-

E-mail address: moorehead2@wisc.edu (M. Moorehead).

chanical and microstructural data are available is ~210 dpa after operation at 400°C in the case of HT9 ferritic-martensitic steel [3].

Due to the inherently slow rate of damage accumulation in present-day test reactors, ion irradiation is widely used to simulate and predict the in-reactor neutron damage generated in materials. While the use of ion irradiation dramatically increases the rate of radiation damage relative to in-reactor conditions (~10<sup>-3</sup> dpa/s versus ~10<sup>-7</sup> dpa/s [4]), the damage layer thickness is typically on the order of micrometers, which restricts the range of mechanical testing and characterization that can be performed to evaluate irradiation damage. Additionally, sample preparation both before and after irradiation can be time consuming due to the time needed to produce samples with an appropriate surface finish for ion irradiation and the potential machining of micromechanical test speci-

<sup>\*</sup> Corresponding author at: 1500 Engineering Dr. ERB 927 Madison, WI 53706, USA.

mens or fabricating transmission electron microscopy (TEM) lamellae using a focused ion beam (FIB). Finally, considering the significant differences in dose rate and energy transfer processes, there is the possibility of ion irradiation producing microstructural changes different from those observed in neutron irradiated materials. However, a nearly equivalent damage microstructure between the two types of irradiation can be achieved by the optimization of ion irradiation parameters. Even with ion irradiation, however, the process for evaluating radiation damage response in new exploratory alloys can remain quite time consuming. This is particularly the case for the emerging field of high-entropy-alloys (HEAs), part of the broader class of compositionally complex alloys (CCAs), which show promise for high irradiation damage tolerance [5-8], but necessitate new approaches to study the almost limitless compositional and microstructural combinations. While the definition of what qualifies as an HEA has expanded since its inception [9] to include non-equimolar alloys and alloys with less than five principle elements [10], there is still debate in the literature over the extents of the HEA space and whether it should include multiphase alloys and less concentrated alloys. To avoid this semantic ambiguity, the term CCA will mainly be used hereinafter, defined as "alloys comprising multiple elements in high concentrations" [11], of which HEAs are a subset.

To accelerate the materials design and qualification process, the work presented in this study employs high-throughput (HTP) techniques, namely additive manufacturing (AM) of compositional arrays, to parallelize the synthesis, irradiation, and characterization of an alloy matrix. While other HTP alloy synthesis techniques exist, such as combinatorial thin-film (CTF) synthesis [12-14], diffusion couples [15,16], and additively manufactured gradients [17-19], the use of additively manufactured compositional arrays [20] has distinct advantages for ion irradiation experiments. Most other HTP synthesis techniques rely on chemical gradients to produce a range of compositions which poses two challenges for irradiation experiments, 1) a specific composition only exists in an infinitesimal point in the gradient and 2) the chemical gradient itself can cause diffusion at elevated temperatures which may obfuscate other radiation-driven diffusion phenomena, such as radiation-induced segregation (RIS). By using in situ alloying via additive manufacturing to produce a compositional array, bulk samples of discrete composition and arbitrary geometry can be made with grain sizes relevant to industrial alloys. This is a clear advantage over techniques like CTF synthesis, which typically produces inherently irradiation-resistant nano-grained microstructures, potentially yielding non-prototypical results.

In this study, to demonstrate the viability and utility of applying an AM-based HTP methodology to radiation-tolerant alloy development, an assortment of CCAs in the Cr-Fe-Mn-Ni alloy system is examined, including several HEAs which have previously shown promising ion and neutron irradiation tolerance [21,22]. From the Cr-Fe-Mn-Ni system, targeted compositions of each pure element, every  $X_{50}Y_{50}$  binary alloy, every  $X_{33}Y_{33}Z_{33}$  ternary alloy, every  $W_{18}X_{27}Y_{27}Z_{27}$  and  $W_{15}X_{35}Y_{15}Z_{35}$  quaternary alloy, and the equimolar alloy,  $Cr_{25}Fe_{25}Mn_{25}Ni_{25}$ , have been examined.

## 2. Methods and materials

Cr-Fe-Mn-Ni compositional arrays produced in this work were synthesized via direct energy deposition (DED) carried out using an Optomec LENS MR-7 equipped with a 1-kW Nd:YAG laser (spot size  $600~\mu m$ ) and four independently controlled powder hoppers. Each hopper was filled with a single elemental powder. Elemental powders used were in the size range of 45-150  $\mu m$  in diameter and were produced via gas atomization, which produces nominally spherical powders. All samples were printed in an argon atmosphere, with  $O_2$  content monitored and maintained below 10 ppm,

on unheated 316 stainless steel build plates, 6.35 mm in thickness, while the laser focus was set to be ~380  $\mu$ m below the surface of the build layer. Since using elemental powders to perform in situ alloying via DED often leads to the incorporation of unmelted elemental powders in the printed alloy matrix [23,24], multiple intermittent laser remelting passes were employed to ensure chemical homogeneity. The printing regime for a single sample (illustrated in Fig. 1) was as follows:

- (1) While flowing powder (mixed in flight), deposit a layer of material with a single rastering pass with the laser over the cross section of the part.
- (2) Without powder flowing, perform one or more rastering passes with the laser over the cross section of the part – entirely remelting the previously deposited layer with each pass.
- (3) Move to next layer height and prepare for next deposition layer.

For each sample in a compositional array, this cycle was repeated for a total of five deposition layers, with a square cross section 10 mm on a side. The printhead was moved vertically 1 mm after each complete deposition + remelt cycle, loosely resulting in a layer thickness of ~1 mm and a total height of ~5 mm for each sample, with some variation as a function of composition. Each sample was printed using two remelting passes (rotated 90°) for each deposited layer and using a hatch spacing of 190  $\mu$ m and a speed of 21.16 mm/s during remelting passes and a hatch spacing of 380  $\mu$ m and speed of 10.58 mm/s during deposition passes. The laser power during remelting and deposition passes was 500 W and 350 W, respectively, when printing each four-element alloy, while laser powers for unary, binary, and ternary alloys were empirically adjusted, based upon the melting point of the composition, to improve the likelihood of successful printing. The laser powers used are summarized in Table 1A in the Appendix section of this paper.

To produce the correct sample compositions, mass flow rate versus hopper auger rotations-per-minute (RPM) calibration curves were first collected. Indeed, when calculated using only a mass balance of the incoming powders, deviations in the printed composition from the target composition are often observed because of the differences in the chemical, morphological, and flow properties of elemental powders. To correct for these deviations, multiple iterations of compositional arrays were printed with the composition of each sample being measured and the mass flow rates calibration curves empirically adjusted by introducing a "retention rate" fitting parameter. Then the relationships between mass flow rate and printed composition are recalculated using a least-squares minimization after each printing iteration. If the terminating surfaces of the as-built samples are flat and nearly coplanar, the composition can be measured quickly and accurately (within  $\pm$  1 at%) via X-ray fluorescence (XRF). However, if there are significant height variations in the different printed samples, composition measurements via energy-dispersive spectroscopy (EDS) were found to be more reliable, albeit slower. A more detailed description of the composition calibration optimization process is given in reference [20]. In this work, all as-built compositions were measured by EDS using a JEOL JSM-6610 scanning electron microscope (SEM). Once satisfactory composition calibration was achieved, whereby deviations between measured composition and target composition were typically less than ~5 at% for each element in each sample (see Table 1A), a compositional array featuring targeted compositions of each pure element, every  $X_{50}Y_{50}$  binary, every  $X_{33}Y_{33}Z_{33}$ ternary, every  $W_{18}X_{27}Y_{27}Z_{27}$  and  $W_{15}X_{35}Y_{15}Z_{35}$  quaternary, and the equimolar Cr<sub>25</sub>Fe<sub>25</sub>Mn<sub>25</sub>Ni<sub>25</sub> was printed, shown in Fig. 2 (note that in this picture the plate was media blasted to remove powders adhered to the surface). All samples were printed using an estimate molar flow rate of 0.3 mols/min, however, due to differences in laser parameters and material behaviors, the final heights

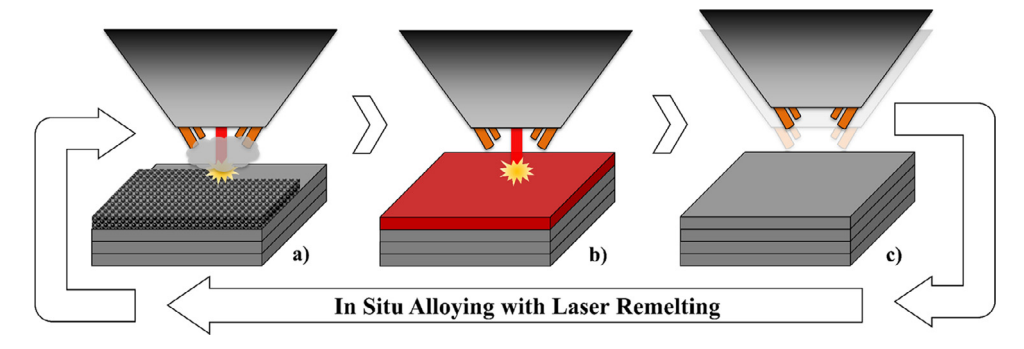


**Fig. 1.** Schematic illustration of in situ alloying via DED with the incorporation of intermittent laser remelting passes (not drawn to scale). (a) Powder, illustrated by the gray plume, is flown through copper nozzles (shown in orange) where it is melted and consolidated by the laser as it passes over the surface of the part. (b) Without powder flowing, the recently deposited layer is remelted by the laser to incorporate any unmelted powders and improve homogeneity. (c) After remelting, the printhead is advanced vertically in preparation for printing the next layer. (For interpretation of the references to color in this figure legend, the reader is referred to the web version of this article.).



**Fig. 2.** Photograph of the as-built Cr-Fe-Mn-Ni array printed on a 316-stainless-steel build plate after media blasting to remove adhered powders. Prior to any machining, sample heights and surface finish as printed vary as a function of composition.

of the samples were varied. Consequently, to aid in further processing, the samples were leveled using wire electrical discharge machining (EDM) to produce coplanar sample heights.

As-fabricated alloys produced by DED, and more generally by additive manufacturing, often exhibit chemical segregation, dislocation structures, and residual stresses resulting from the initial solidification process during the deposition of a given layer. These effects are further influenced by the solid-state heat treatment that will inevitably occur by the thermal cycling caused by the melting of the subsequently deposited layers [25]. To alleviate variations in these effects in the different printed alloys, the entire compositional array was homogenized in a water-cooled Materials Research Furnaces (MRF) vacuum furnace (base pressure  $\sim 10^{-6}$ torr) at 1000°C for 24 hours followed by furnace cooling to room temperature at an average cooling rate of approximately 1°C/s. The temperature of 1000°C was selected as the highest temperature attainable without inducing insipient melting in any of the printed alloys, which is dictated by the relatively low melting point of the MnNi binary alloy (~1020°C) [26]. After the homogenization treatment, the composition of each sample was measured using a handheld SciAps X-200 series XRF detector. The XRF (separately calibrated against EDS) was employed as a high throughput method for compositional analysis on multiple alloy samples. The equilibrium phases of each measured sample composition at 1000°C were calculated using the CALPHAD method, via the Pandat software and the PanHEA thermodynamic database. The entire compositional array was mechanically polished progressively from 120 through 1200 SiC grit papers, followed by polishing with  $3-\mu m$ and 1- $\mu$ m diamond suspensions and finally with 0.04- $\mu$ m colloidal silica to produce surface finish required for ion irradiation in accor-

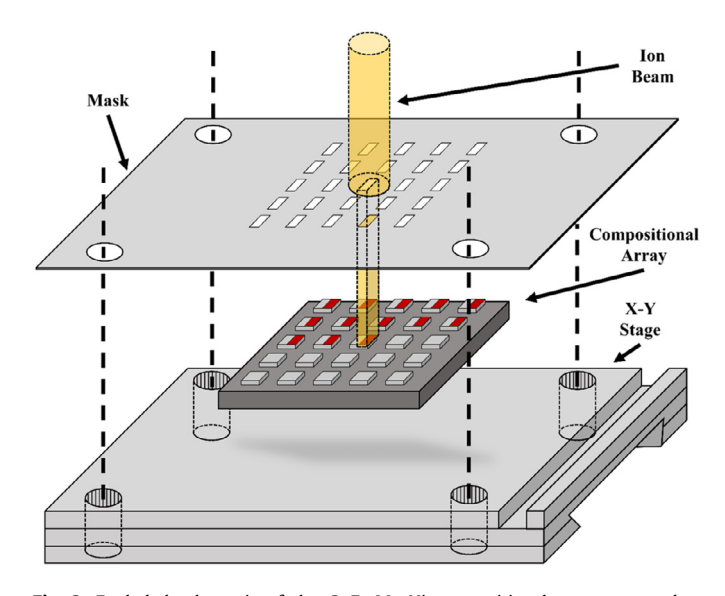


**Fig. 3.** Exploded schematic of the Cr-Fe-Mn-Ni compositional array mounted to custom XY sample stage. Half of each sample in the compositional array is masked by Al foil.

dance with ASTM E521-96 [27]. Surface roughness measurements were performed using a Zygo New View white-light interferometer.

Heavy-ion irradiation was performed at the University of Wisconsin Ion Beam Laboratory (UW-IBL) using a defocused beam of 4-MeV Ni<sup>2+</sup> ions at room temperature. Prior to irradiation, the compositional array was affixed to a custom XY stage, large enough to accommodate the size of the plate. Half of each sample was masked by an Al-foil mask to preserve half of each sample in the unirradiated condition, as illustrated in Fig. 3. To calculate the fluence necessary to produce a target damage level of 50 dpa at the damage peak, the quick Kinchin-Pease (KP) calculation mode was used in SRIM and displacement energies of each element were set to be 40 eV while the lattice binding energy and surface binding energy were each set to 0 eV, as discussed in reference [28]. Since the average masses of Cr, Fe, Mn, and Ni are similar (with pure nickel and chromium representing the largest deviations of  $\pm$  6% from the average), displacement and binding energies of each element were treated as identical, and the densities of each alloy are comparable (as most alloys examined were predicted to be either mostly or entirely face-centered cubic (FCC) by CALPHAD). To simplify the irradiation experimental setup, each alloy was irradiated to the same fluence of 4-MeV Ni<sup>2+</sup> calculated to produce a peak damage of 50 dpa in equimolar CrFeMnNi, which was found

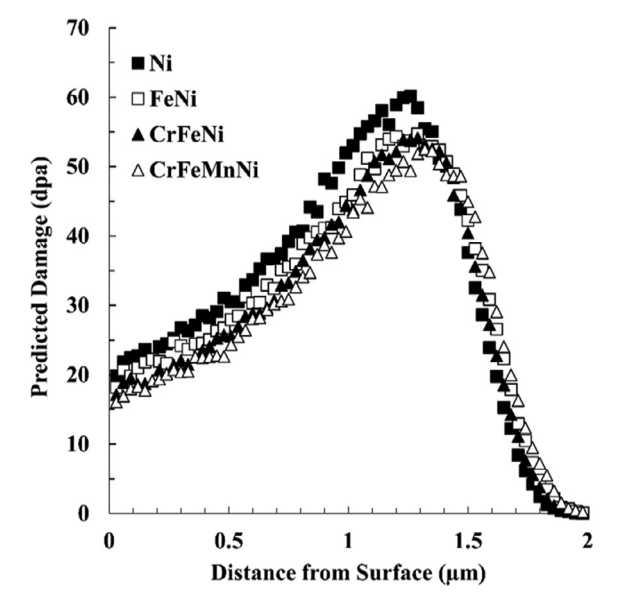


Fig. 4. Damage profiles calculated from SRIM data of various equimolar alloys irradiated with 4-MeV Ni $^{2+}$  ions to a fluence of 5.33  $\times$   $10^{16}$  ions/cm $^2$ .

to be  $5.33 \times 10^{16}$  ions/cm<sup>2</sup>. Fig. 4 shows the damage profiles in four equimolar alloys in the Cr-Fe-Mn-Ni composition space after a fluence of  $5.33 \times 10^{16}$  ions/cm<sup>2</sup> using 4-MeV Ni<sup>2+</sup> ions in which the damage profiles appear more similar with increasing compositional complexity.

Following ion irradiation, X-ray diffraction (XRD) studies were performed, using a Bruker D8 Discovery X-ray diffractometer equipped with a Cu K-alpha X-Ray source, with a spot size of 0.1 mm, and an automated sample stage. The small X-ray spot size and the thickness of each printed sample (several millimeters) ensure that individual samples can be illuminated by X-rays without generating additional signal from the stainless-steel substrate or other nearby samples. XRD was performed on both the irradiated and unirradiated regions the samples to identify any radiation induced phase changes, including potential precipitate dissolution from ballistic mixing, as well as to compare the phases in the unirradiated regions with CALPHAD predictions. The latter point is particularly critical for alloy design purposes [29,30]. Nanoindentation measurements were performed along a 6-mm-long line in the center of each sample crossing the interface between the unirradiated/irradiated regions to evaluate radiation-induced hardness changes. Nanoindentation measurements were performed using a Bruker Hysitron TI-950 Triboindenter, equipped with a Berkovich tip. All measurements were performed using load control mode in which the maximum applied load was fixed at 6000  $\mu$ N. The experiment was performed into two steps; the loading step, where the load is applied to push the indenter into the material at a loading rate of 1 mN/s until it reaches the maximum specified load, followed by the unloading step, where the indenter is drawn back to its original position. Uncertainty in the nanoindentation measurements primarily originates from estimation of the contact area between the indenter and the material, and it is generally accepted to be ~5% or less [31]. For each sample, a line scan of indents was performed across the irradiation interface with 200 µm lateral step size. Samples were characterized in the as-built state and after homogenization + irradiation using JEOL JSM-6610 scanning electron microscope (SEM) equipped with EDS. ImageJ® was used to threshold SEM images and identify individual pores in the samples to determine pore size distributions and total porosity by calculating the area fraction.

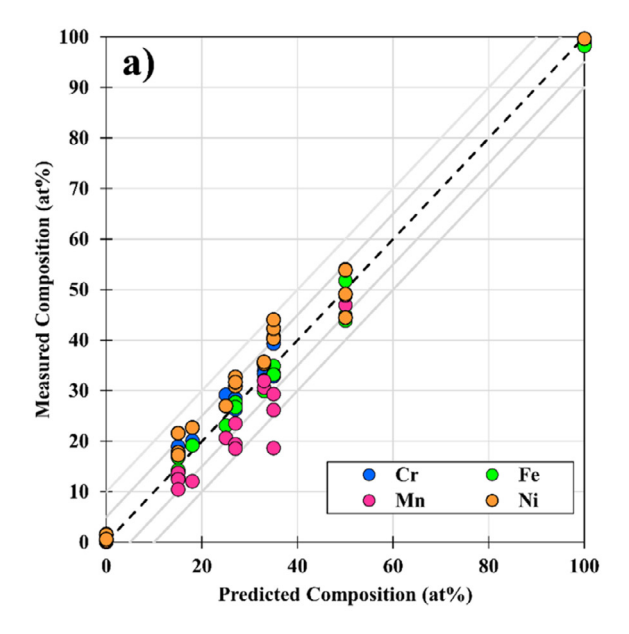
## 3. Results

In order to perform accurate characterization of samples using XRD and XRF, a minimum area of sample uniformity is needed based on the spot size of the X-ray source from each technique. In this study, the spot size of the XRF gun, a circular area approximately 6 mm in diameter, dictated the minimum geometry necessary for measurements. As a result, three samples, shown in Fig. 2, have not been included for analysis namely the sample in Row 1 / Column 3, Row 2 / Column 1, and Row 3 / Column 1, corresponding to target compositions of pure Mn, CrMn, and CrFeMn, respectively. In general, high-Mn compositions presented a challenge to printing due to volatilization and this problem is often exacerbated when paired with higher melting point elements (e.g. Cr), which themselves necessitate higher laser powers to melt sufficiently. For ease of discussion, samples will be referred to hereinafter by their compositions, in at%, as measured by XRF after homogenization.

## 3.1. Alloy compositions

The compositions of the alloys from the Cr-Fe-Mn-Ni compositional array are plotted against their as-built targeted compositions in Fig. 5 in both the as-built and homogenized conditions. While XRF is the preferred method for measuring chemical composition for these samples due to its speed, the variations of height and surface finish of the samples in the as-built condition preclude the use of XRF since the snout of the XRF gun must be placed flat against the measurement surface. To remedy this, chemical composition in the as-built condition was measured using EDS while after homogenization and leveling via wire EDM, XRF was used. For materials with extensive standard libraries (e.g. steels), XRF and EDS have been found to be in close agreement ( $\pm 1$  at%), thus, the chemical compositions measured using these two techniques is used interchangeably for the Cr-Fe-Mn-Ni alloys produced in this study. The measured compositions were originally within ~5 at% of their targeted compositions, with only one outlier deviating by more than 10 at%. After homogenization at 1000°C for 24 hours under vacuum, a large decrease in the Mn content was observed which scaled with the initial Mn content of the alloy. The suspected cause for the loss of Mn during homogenization is the relatively high vapor pressure of Mn at  $1000^{\circ}$ C, approximately  $10^{-2}$  torr [32], which is several orders of magnitude larger than the base pressure of the MRF vacuum furnace used for heat treatment, which was approximately  $10^{-6}$  torr.

In addition to Mn loss during the homogenization treatment, effects of additive manufacturing geometry on the composition were observed in the printing of pure Cr, where rather than measuring close to 100 at% Cr, the composition measured by XRF was found to be Cr<sub>74</sub>Fe<sub>21</sub>Mn<sub>1</sub>Ni<sub>4</sub>. The presence of Fe, Mn, and Ni in the measured ratios inside the Cr sample are likely due to substantial intermixing of the printed Cr and the SS-316 build plate caused by the comparatively short build height of the Cr sample, seen in the top left corner of the build plate in Fig. 2. Since the penetration depth of the electrons used to measure the composition via EDS in the as-built condition is substantially shorter than that of the X-rays used in XRF, it is unclear whether the intermixing of the Cr with the SS-316 build was caused primarily during printing or as a result of the homogenization heat treatment. In any case, the Cr sample serves to motivate the need to build up samples far beyond the surface of the substrate to avoid effects from the substrate and the interface region. Of course, one could use the substrate material as an alloying element, which has been successfully demonstrated as a high-throughput in situ alloying technique in [33].



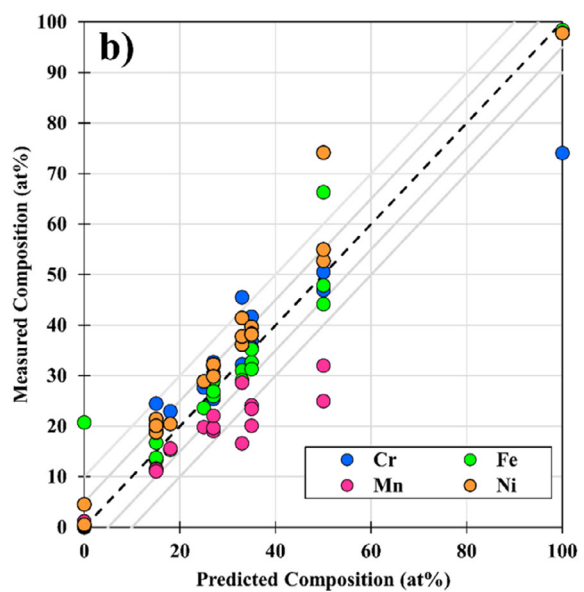


**Fig. 5.** Measured composition versus predicted composition for each element in each sample of the Cr-Fe-Mn-Ni compositional array measured by (a) EDS in the as-built state and by (b) XRF in the homogenized state.

## 3.2. Phases

XRD was used to examine the phase distribution of each sample from the Cr-Fe-Mn-Ni compositional array in both the irradiated and unirradiated regions. As may be expected from a room-temperature irradiation, the XRD patterns in the irradiated regions of each sample appear very similar to their unirradiated counterparts indicating no substantial new phases. Each alloy was found to consist of either a single-phase body-centered cubic (BCC) structure, a single-phase face-centered cubic (FCC) structure, or a combination of FCC and BCC phases. To compare with the expected phases of the Cr-Fe-Mn-Ni system from CALPHAD, compositions spanning the entire Cr-Fe-Mn-Ni composition space were simulated using the Pandat high-throughput calculation (HTC) function, with a step size of 5 at%, at 1000°C – the temperature used for homogenization of the compositional array. The results from the CALPHAD HTC are shown in Fig. 6 with the exper-

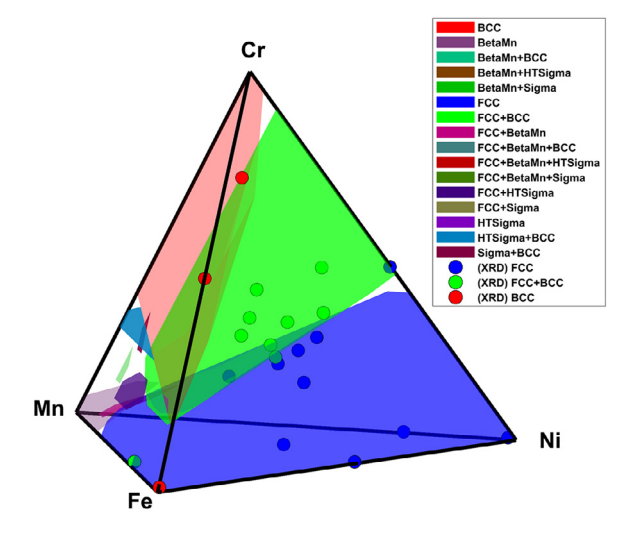


**Fig. 6.** HTC CALPHAD equilibrium phases of the Cr-Fe-Mn-Ni composition space at  $1000^{\circ}\text{C}$  with experimental XRD results overlaid.

imental XRD results overlaid. The phases identified experimentally via XRD are in remarkable agreement with the equilibrium phases predicted by CALPHAD simulation. In each of the multiphase (FCC+BCC) HEAs, the FCC phase is slightly enriched in Ni while the BCC phase is significantly enriched in Cr. The boundary between the FCC and FCC+BCC regions predicted by CALPHAD, where the most experimental data is present, matches the experimental data within a few at%. These variations are close to the uncertainty of the XRF measurements of approximately  $\pm$  1 at%. However, two notable outliers were observed: pure Fe and Fe<sub>67</sub>Mn<sub>33</sub>. At 1000°C, both pure Fe and Fe<sub>67</sub>Mn<sub>33</sub> were expected to be a single FCC phase but were instead observed experimentally to be BCC, and FCC + BCC, respectively. Evidently, these two alloys underwent solid-state phase transformation as a result of the noninstantaneous cooling rate of the compositional array following the homogenization heat treatment since pure Fe is expected to transition from FCC to BCC at approximately 912°C and Fe<sub>67</sub>Mn<sub>33</sub> is similarly predicted to become FCC + BCC at lower temperatures.

#### 3.3. Microstructural characterization

After irradiation, samples from the compositional array were examined using SEM and EDS. The irradiated region of each sample was distinguishable from the unirradiated region by its darker contrast when imaged using an in-lens secondary-electron detector, which may be caused by changes in surface morphology or deposition of neutral carbon atoms during irradiation [34]. However, besides this slight change in contrast, no microstructural differences were observed between the unirradiated and irradiated regions of the samples. To highlight the different microstructures observed in the Cr-Fe-Mn-Ni system, Fig. 7 shows the SEM images and EDS chemical maps taken from the unirradiated region of three CCAs,  $Cr_{19}Fe_{31}Mn_{11}Ni_{39}$ ,  $Cr_{28}Fe_{23}Mn_{20}Ni_{29}$ , and  $Cr_{42}Fe_{17}Mn_{20}Ni_{21}$ with approximate Cr:Ni ratios of 1:2, 1:1, and 2:1, respectively. For Cr<sub>19</sub>Fe<sub>31</sub>Mn<sub>11</sub>Ni<sub>39</sub>, a single chemically homogeneous phase is observed with fine uniformly distributed pores with an average area of 0.15  $\pm$  0.10  $\mu$ m<sup>2</sup> and a total porosity of 0.55%. With increasing Cr content and decreasing Ni content, Cr<sub>28</sub>Fe<sub>23</sub>Mn<sub>20</sub>Ni<sub>29</sub> shows the formation of BCC Cr-rich precipitates uniformly distributed throughout the FCC matrix and an increase in both the average pore size and total porosity which was measured to be  $0.20 \pm 0.16 \ \mu \text{m}^2$  and 1.35%, respectively. Further increase in the Cr:Ni ratio, in the case of Cr<sub>42</sub>Fe<sub>17</sub>Mn<sub>20</sub>Ni<sub>21</sub>, leads to an increase in the Cr-rich BCC phase fraction, which rather than forming discrete

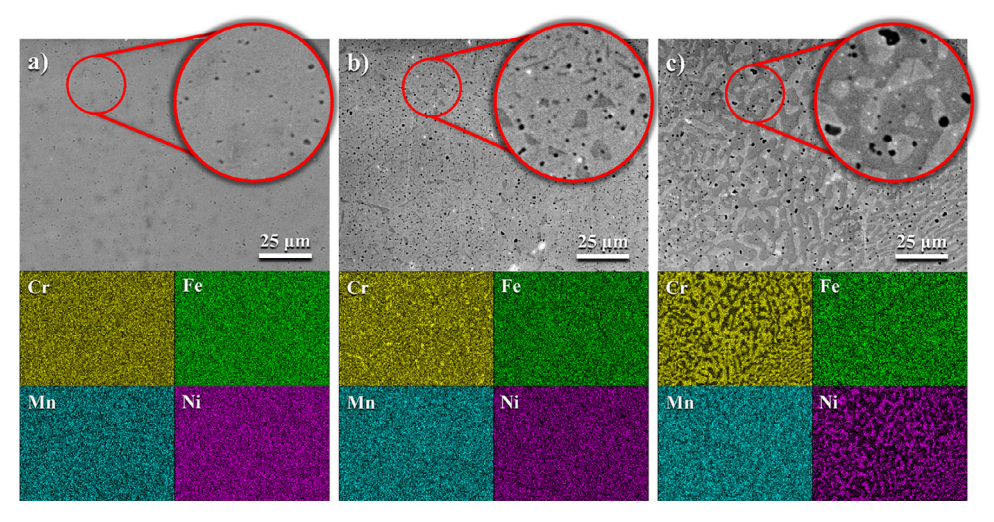


**Fig. 7.** SEM images and EDS chemical maps from the unirradiated regions of (a)  $Cr_{19}Fe_{31}Mn_{11}Ni_{39}$  (b)  $Cr_{28}Fe_{23}Mn_{20}Ni_{29}$ , and (c)  $Cr_{42}Fe_{17}Mn_{20}Ni_{21}$ . Each alloy consists of a primary FCC phase with an increasing amount of the BCC Cr-rich phase (dark contrast) from (a) to (c). Insets are provided in red circles at a magnification 3x greater than the base images to highlight the porosity distributions. (For interpretation of the references to color in this figure legend, the reader is referred to the web version of this article.).

precipitates in an FCC matrix instead forms a globular interconnected network intertwined with the FCC phase. Relative to the previous two alloys, the average pore size and total porosity was also measured to increase in  $\text{Cr}_{42}\text{Fe}_{17}\text{Mn}_{20}\text{Ni}_{21}$  to  $0.34\pm0.34~\mu\text{m}^2$  and 1.95%, respectively. Overall, from the EDS chemical mapping, Cr and Ni are observed to segregate more strongly than Fe and Mn during this phase separation, and both the pore size and total porosity area fraction was observed to increase with increasing Cr-rich BCC phase fraction.

## 3.4. Hardness

While phenomena such as void swelling, RIS, and radiation-induced precipitation would not be expected in Cr-Fe-Mn-Ni alloys irradiated at room temperature, due in part to the lack of vacancy mobility, radiation hardening from point defects and from the formation of self-interstitial atom (SIA) clusters would be expected [35]. Fig. 8 shows the nanoindentation line profiles of two less compositionally complex single-phase BCC solid-solution alloys. Here, a sharp step increase in hardness is observed for  $\rm Cr_{51}Fe_{49}$  from ~3.5 GPa to ~5 GPa between the unirradiated and irradiated region while the comparatively softer Fe shows a more gradual increase from ~1.75 GPa to ~3.25 GPa. The gradual increase is likely caused by the Al-foil mask interface not being quite perpendicular to the nano-indentation line scan.

Alongside the single-phase BCC alloys, many single-phase FCC alloys were examined, including several single-phase FCC CCAs, where evidence of irradiation hardening was clearly visible. Fig. 9 shows a pair of typical load-versus-displacement curves, generated from nanoindentation of the unirradiated and irradiated regions of  $Cr_{20}Fe_{35}Mn_{24}Ni_{20}$ . To achieve the target load of 6000  $\mu$ N, a displacement of ~300 nm is necessary in the unirradiated condition while the same load is reached after a displacement of ~250 nm in the irradiated condition, corresponding to an increase in hardness from ~2.5 GPa to ~3.5 GPa after irradiation. A comparison of the hardening behavior of various FCC CCAs is shown in Fig. 10, which includes the nanoindentation line profiles centered on the unirradiated/irradiated interface of Cr<sub>20</sub>Fe<sub>35</sub>Mn<sub>24</sub>Ni<sub>20</sub>, Cr<sub>19</sub>Fe<sub>31</sub>Mn<sub>11</sub>Ni<sub>38</sub>, and Cr<sub>23</sub>Fe<sub>26</sub>Mn<sub>19</sub>Ni<sub>32</sub>. In the unirradiated region, the hardness values of the FCC CCAs range from ~2.5-3.25 GPa, while after irradiation the hardness values range from ~3.5-4.75 GPa, thus exhibiting a slight improvement over the BCC Fe and CrFe alloys.

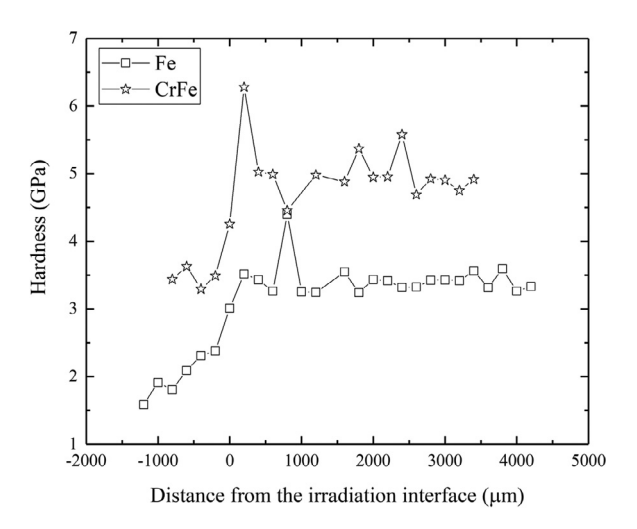


**Fig. 8.** Hardness profiles across the unirradiated/irradiated interface of select single-phase BCC alloys measured via nanoindentation. Since the unirradiated region for these two alloys was only sampled by the first ~5 point of each scan, hardness values have been plotted as a function of distance from the sample edge for clarity.

In each of the single-phase alloys, the hardness before and after irradiation can be readily determined from the individual nanoindentation line scans. However, for the two-phase (FCC+BCC) CCAs, even if a step increase in hardness across the unirradiated/irradiated interface is observed, the scatter in hardness values within a region is often substantial. This makes it difficult to discern the absolute hardness of the individual phases. Since nanoindentation measurements probe a finite interaction volume several micrometers in all directions [31], the size and spatial distribution of second phases affect the hardness measured from a single point and can produce a distribution of hardness values for a two-phase system rather than two discrete hardness values, one for each phase. To try and visualize the data from the multiphase alloys in a meaningful way, Fig. 11 shows histograms of the unirradiated and irradiated areas, respectively, pooled from every alloy examined where the interface between the unirradiated/irradiated interface is discernable in the hardness data. A kernel smoothing function was applied to the raw hardness data to produce a probability density function (PDF) for both conditions; the bin size for

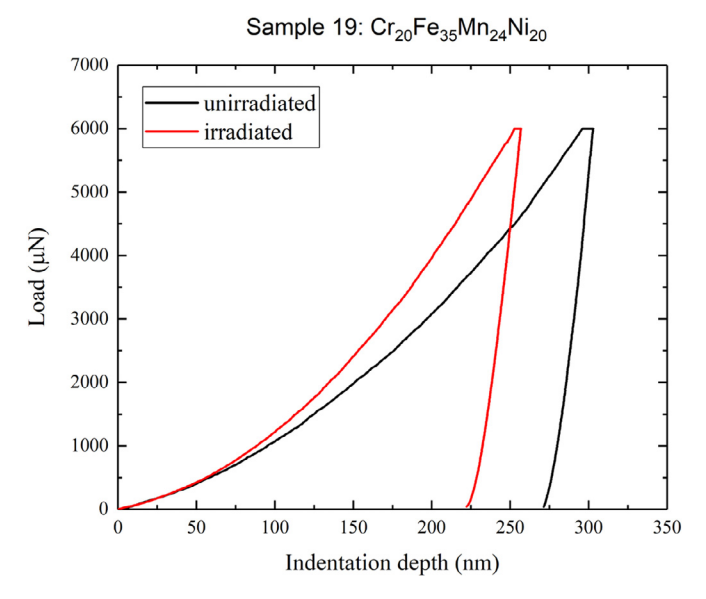
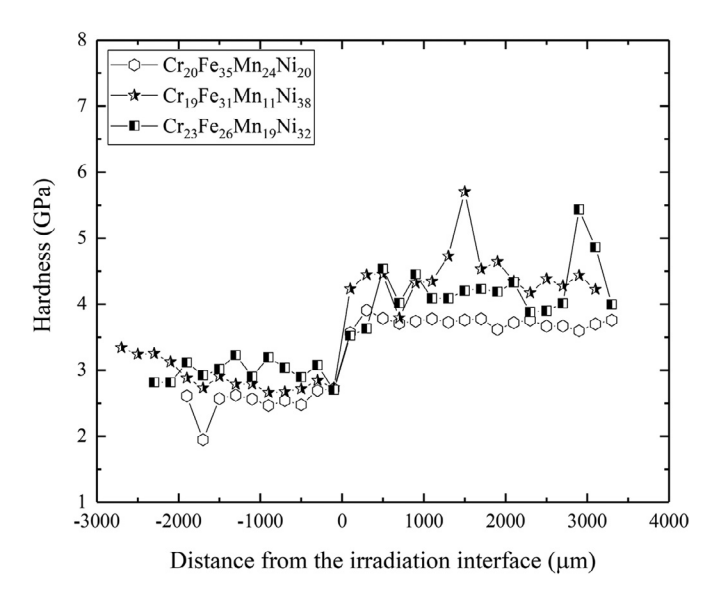


Fig. 9. Representative load vs. displacement curves from the unirradiated and irradiated regions of the FCC CCA  $Cr_{20}Fe_{35}Mn_{24}Ni_{20}$ .



**Fig. 10.** Hardness profiles across the unirradiated/irradiated interface for several single-phase FCC CCAs measured via nanoindentation.

both the histograms and the kernel smoothing functions was set to 0.25 GPa. In the unirradiated histogram (Fig. 11a), two primary groups of hardness values were observed centered at 3 GPa and 4.5 GPa, which can generally be attributed to the Ni-rich FCC phase and the Cr-rich BCC phases measured in many of these alloys by XRD (compositions inferred from CALPHAD), with the exception of a few of the unary and binary alloys (e.g. Fe, Fe<sub>67</sub>Mn<sub>33</sub>). After irradiation (Fig. 11b), the two original groups of hardness data merged into a single group of hardness values, centered at approximately 4.25 GPa. Had the FCC and BCC phases both hardened to the same extent, the same bimodal hardness distribution seen in the unirradiated condition would be expected in the irradiated condition (only offset to higher hardness values). However, this was not observed suggesting that the Cr-rich BCC phase in the two-phase Cr-Fe-Mn-Ni CCAs is more resistant to irradiation hardening than the Ni-rich FCC phase.

## 4. Discussion

To the best of the authors' knowledge, this study represents the first time an additively manufactured compositional array has been irradiated in a high-throughput manner. Producing compositional arrays using in situ alloying via additive manufacturing is, however, not without its challenges. Specifically, minimizing porosity and maintaining compositional accuracy after heat treatment are two area whose improvement would have a substantial impact on the robustness and utility of additive manufacturing as a high-throughput irradiation tolerance screening technique.

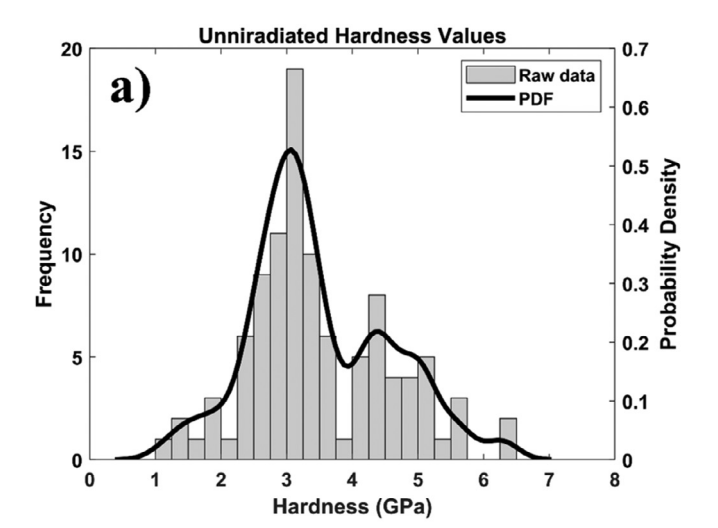
Prior to homogenization, some loss of Mn from the compositional array was anticipated and the depth of the Mn-depleted layer was estimated using isotope tracer diffusion data from the well-studied austenitic 316 stainless steel (SS-316) system, as a surrogate for the Cr-Fe-Mn-Ni CCAs of which little diffusion data is available for in the literature. From reference [36], the lattice diffusion coefficient of Mn in SS-316 at 1000°C was calculated to be 8.84  $\times$  10<sup>-16</sup> m<sup>2</sup>/s. Using the characteristic diffusion length as an estimate suggests a Mn-depleted depth of approximately 17.5  $\mu$ m in thickness under the homogenization treatment used in this study. This thickness was considered negligible when compared to the amount of material removed during mechanical grinding and polishing after heat treatment. However, while this assumption remains valid for the low-Mn alloys, it may not be true for higher Mn contents. The cause of the increased Mn depletion for alloys with higher Mn content is likely due the depressed melting point of high-Mn alloys, which causes the homogenization temperature to translate to a substantially higher homologous temperature for these alloys. This would of course lead to a lower vacancy activation energy for the high-Mn alloys, resulting in higher diffusion coefficients. For example, using the Pandat software with the PanHEA database, the melting point (T<sub>mp</sub>) of equimolar CrFeMnNi was calculated to be 1268°C while the melting point of Mn<sub>50</sub>Ni<sub>50</sub> was calculated to be 1045°C corresponding to homologous temperatures of  $0.83T_{mp}$  and  $0.97T_{mp}$ , respectively. As such, the measured compositions of equimolar CrFeMnNi and Mn<sub>50</sub>Ni<sub>50</sub> after homogenization were found to be Cr<sub>27</sub>Fe<sub>24</sub>Mn<sub>20</sub>Ni<sub>29</sub> and Mn<sub>25</sub>Ni<sub>75</sub>, respectively. From this finding, unless homogenization heat treatments can be performed at elevated pressures without substantial oxidation, it is recommended that Mn content is kept below ~25 at% to prevent substantial volatilization.

Each sample in the compositional array has some degree of porosity, as measured by SEM. It is necessary to understand both the distribution and the causes for this porosity so that it can be minimized as this HTP process is further developed. Few materials synthesis techniques are able to produce materials at 100% of their theoretical density, however, laser-based additive manufacturing is particularly prone to introducing pores into printed material when laser parameters are not optimized [37]. While there are many sources of porosity in additively manufactured materials, two of the most common sources in DED are keyhole (metalvaporization) porosity and entrapped-gas porosity, both of which become more common with increasing laser power. Both types of pores stem from fluid instabilities in the melt pool near the metal-vapor depression directly under the laser, which can trap metal vapor from the deposited material and/or inert gas from the build environment upon solidification. Pores containing metal vapor quickly become evacuated as the vapor condenses on cooling, however, pores with entrapped inert gases maintain an internal gas pressure on cooling. In addition to porosity introduced during synthesis, heat treatment can also produce porosity by the Kirkendall effect due to differences in diffusion coefficients between the dendritic/interdendritic regions in the solidification structure or during the formation and evolution of secondary phases. To remove these pores, hot isostatic pressing (HIP) is often used, which

is effective at closing evacuated pores including metal-vapor pores and Kirkendall voids. However, HIPping is less effective at removing entrapped gas pores due to the internal gas pressure and low solubility of inert gases, such as argon, in solid metals [38]. To assess the role of the Kirkendall effect on porosity of the samples in the Cr-Fe-Mn-Ni compositional array, the porosity in the FCC CCAs (Fig. 7) can be compared to the porosity of the pure Fe sample (Sample #2). The pure Fe sample was measured to have a total porosity of 0.48% with an average pore size of 0.12  $\pm$  0.06  $\mu$ m<sup>2</sup>. Since this sample consists of a single element, there should be no additional porosity caused by Kirkendall voiding during heat treatment. Therefore, this level of porosity can be considered a baseline for samples in the compositional array. By comparison, the total porosity in the single-phase FCC CCA Cr<sub>19</sub>Fe<sub>31</sub>Mn<sub>11</sub>Ni<sub>39</sub> was measured to be 0.55% with an average pore size of 0.15  $\pm$  0.10  $\mu\text{m}^2\text{,}$ which is quite close to the baseline level. This suggests minimal Kirkendall voiding occurs as a result of the elimination of chemical segregation from the solidification structure upon homogenization. In contrast, as the Cr content is increased, leading to the formation of a BCC phase in  $Cr_{28}Fe_{23}Mn_{20}Ni_{29}$  and  $Cr_{42}Fe_{17}Mn_{20}Ni_{21}$ , the total porosity increases to 1.35% and 1.95%, respectively. Moreover, in addition to the population of submicron pores distributed uniformly throughout every printed sample, Cr<sub>42</sub>Fe<sub>17</sub>Mn<sub>20</sub>Ni<sub>21</sub> (shown in Fig. 7c) features an additional population of larger pores positioned at the interface between the FCC and BCC phases. This would indicate substantial Kirkendall voiding increasing with the BCC phase fraction. Since a large source of pores in the two-phase CCAs appears to be Kirkendall voiding from the FCC+BCC phase separation, the total porosity of these samples, and future compositional arrays, should be able to be reduced substantially with a HIP treatment.

The assortment of Cr-Fe-Mn-Ni alloys irradiated in this campaign offer several insights into both the hardening response of this class of CCAs and the implications of using high-throughput techniques in the development of radiation-tolerant materials. Firstly, radiation-induced hardening was observed in both FCC and BCC CCAs as well as several multiphase (FCC+BCC) CCAs. However, the degree of hardening is dependent on both the crystal structure and the composition of the phase. For example, while the irradiated pure Fe and CrFe binary alloy show an average increase in hardness of ~1.5-2 GPa (Fig. 8), the hardness of the Cr-rich BCC phase present in the two-phase CCAs showed negligible change in hardness (Fig. 11). In contrast, the magnitude of the change in hardness and the average hardness of the single-phase FCC CCAs (Fig. 10) seem to be relatively insensitive to modest changes in concentrations of Fe, Mn, and Ni in the alloys, whose hardening due to irradiation all ranged around ~1-1.5 GPa. Overall, the hardness values of the single-phase FCC CCAs before and after irradiation in this work are in good qualitative agreement with hardness measurements from low-temperature neutron irradiations of a comparable Cr-Fe-Mn-Ni FCC HEA [22], which also was measured to have an initial hardness ~3 GPa and a change in hardness of ~1.5 GPa after neutron irradiation to 1 dpa - a damage level above which radiation-induced hardening would be expected to saturate [39]. This builds confidence in the validity of using additively manufactured compositional arrays to predict the response of CCAs under reactor conditions.

To understand the exact atomistic mechanisms underpinning the irradiation response of a material typically requires the use of TEM or equally in-depth and time-consuming techniques. However, this is expressly not the purpose of employing HTP screening techniques. Instead, HTP techniques, including the ones employed in this study, enable researchers to expand their search ranges and explore alloy compositions that would otherwise be time and cost prohibitive. Incidentally, the HTP synthesis, irradiation, and characterization methodology presented in this study is an embodi-



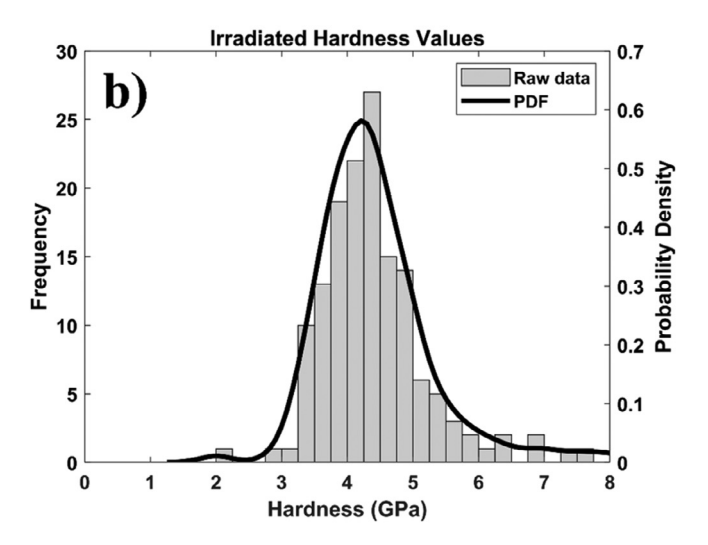


**Fig. 11.** Histograms of the hardness values measured from (a) the unirradiated region and (b) the irradiated region of each alloy via nanoindentation. Alloys in which the unirradiated/irradiated interface was undiscernible have been omitted.

ment of the Pareto principle, wherein 80% of the challenge can be overcome with 20% of the effort. While HTP techniques will always need to be coupled to more precise *low-throughput* techniques, their implementation serves as an enabling approach to accelerate the development of CCAs and novel materials for advanced nuclear technologies in general.

The time savings resulting from HTP techniques cannot be overstated. To quantify this assessment, one needs to consider the time needed to synthesize, irradiate, and characterize 25 alloys using traditional approaches. To arc melt a chemically homogeneous button, careful weighing of the precursor elements must be performed followed by several melting iterations with intermediate flipping of the melted button, which often requires the arc melter to be brought back to atmospheric pressure to flip the button and/or clean the chamber depending on the type of system and materials being melted. Optimistically, this entire process may take ~1-2 hours per alloy. By comparison, each alloy in the Cr-Fe-Mn-Ni compositional array featured in this study took approximately 10 minutes to print with less than 30 seconds between switching compositions, meaning the array of 25 compositions was able to be synthesized, conservatively, in less than 5 hours - representing a time savings between fivefold and tenfold. Similar time savings are achieved for sample preparation (because an entire compositional

array can be polished simultaneously), during irradiation, where only one vacuum cycle between atmospheric pressure and ultrahigh vacuum is necessary to load the compositional array, and for characterization techniques where the regular spacing of samples in the compositional array allows a user to take full advantage of automated data collection (e.g. in the case of XRD and nanoindentation), as has been demonstrated in this study.

#### 5. Conclusions and future work

Using DED to produce an array of CCAs, which were subsequently irradiated and characterized, additive manufacturing has been demonstrated to be an enabling technology for the highthroughput (HTP) assessment of the irradiation properties of alloys, specifically for the Cr-Fe-Mn-Ni family of CCAs, which show promise as radiation-tolerant materials. CALPHAD simulations of the Cr-Fe-Mn-Ni composition space have been demonstrated to accurately predict the phase distributions of concentrated alloys after homogenization at 1000°C, as confirmed by XRD. In total, 25 alloy compositions were rapidly synthesized and irradiated, 23 of which were of sufficient quality to be characterized using XRF, XRD, and nanoindentation. Radiation-induced hardening of several CCAs was measured, with hardness increases ranging from ~1-1.5 GPa, which is comparable to hardening observed in neutron-irradiated Cr-Fe-Mn-Ni HEAs in the literature. In general, the combination of HTP techniques in this study including additive manufacturing, CALPHAD modeling, and automated characterization techniques, has demonstrated immense time savings over conventional exploratory alloy development processes. Assessment of compositional accuracy and porosity distributions in the additively manufactured compositional array has provided guidance for future printing campaigns, including reducing Mn content below ~25 at% and adding a HIP treatment to eliminate metal-vapor pores from manufacturing and Kirkendall voids from heat treatment. Future work will focus on performing ion irradiation at higher temperatures to promote other radiation-induced phenomena such as void swelling, RIS, and phase changes also to be characterized using HTP methods, as well as covering a larger compositional space in this alloy system and others less explored.

## Data availability

The raw/processed data required to reproduce these findings will be made available upon request.

## **Declaration of Competing Interest**

The authors declare that they have no known competing financial interests or personal relationships that could have appeared to influence the work reported in this paper.

## **CRediT authorship contribution statement**

Michael Moorehead: Conceptualization, Methodology, Formal analysis, Investigation, Writing - original draft, Writing - review & editing, Visualization. Phalgun Nelaturu: Methodology, Formal analysis, Investigation. Mohamed Elbakhshwan: Methodology, Formal analysis, Investigation, Visualization. Calvin Parkin: Formal analysis, Investigation. Chuan Zhang: Software, Validation. Kumar Sridharan: Conceptualization, Supervision, Writing - review & editing, Funding acquisition. Dan J. Thoma: Resources, Supervision, Writing - review & editing, Project administration. Adrien Couet: Conceptualization, Supervision, Writing - review & editing, Project administration, Funding acquisition.

for compositions, as-built compositions measured via EDS, measured compositions via XRF after homogenization, phases predicted by CALPHAD, and experimentally observed phases via XRD manufactured Cr-Fe-Mn-Ni compositional array **Tabulated** 

			Target	Target Composition (at%)	sition (a	t%)	As-Buil	As-Built Composition (at%)	sition (a	(%:	Compo	sition afi	er Hom	Composition after Homogenization (at%)	Simulated at 1000°C	After Homogenization
Sample #	Deposition Laser Power (W)	Remelt Laser Power (W)	b		Mn	ž	Ċ	Fe	Mn	ï	J	Fe	Mn	ïZ	Phases (CALPHAD)	Phases (XRD)
1	550	700	100	0	0	0	0.66	0.3	0.3	0.3	74.1	20.8	9.0	4.6	BCC	BCC
2	400	550	0	100	0	0	8.0	98.3	0.7	0.3	1.1	98.4	0.2	0.2	FCC	BCC
3	200	350	0	0	100	0					,					1
4	350	500	0	0	0	100	0.1	0.2	0.1	99.7	9.0	0.4	1.2	87.8	FCC	FCC
2	200	650	20	20	0	0	53.9	43.9	0.7	1.5	9.09	47.9	1.1	0.4	BCC	BCC
9	350	500	20	0	20	0	,	,			,	,				1
7	450	009	20	0	0	20	54.1	9.0	6.0	44.5	47.0	0.1	0.2	52.8	FCC+BCC	FCC
8	250	400	0	20	20	0	9.0	51.8	47.0	9.0	1.1	66.3	32.0	0.5	FCC	FCC+BCC
6	350	500	0	20	0	20	9.0	44.9	9.0	53.9	0.3	44.2	0.5	55.0	FCC	FCC
10	200	350	0	0	20	20	0.3	1.7	48.9	49.2	0.4	0.4	25.0	74.2	FCC	FCC
11	400	550	33	33	33	0					,	,				1
12	450	009	33	33	0	33	33.9	30.0	0.5	35.6	32.2	31.1	0.5	36.2	FCC	FCC
13	350	500	33	0	33	33	33.4	0.7	30.6	35.4	45.6	0.0	16.6	37.8	FCC+BCC	FCC+BCC
14	250	400	0	33	33	33	0.2	32.1	32.0	35.7	8.0	29.1	28.7	41.5	FCC	FCC
15	350	500	25	25	25	25	29.2	23.1	20.7	27.0	27.7	23.6	19.8	28.9	FCC	FCC+BCC
16	350	200	35	35	15	15	33.5	34.9	13.8	17.8	36.9	32.7	11.6	18.8	FCC+BCC	FCC+BCC
17	350	200	35	15	35	15	39.4	14.0	29.3	17.3	41.7	16.7	20.1	21.5	FCC+BCC	FCC+BCC
18	350	500	35	15	15	35	32.9	14.3	12.5	40.3	35.6	13.3	11.5	39.7	FCC+BCC	FCC+BCC
19	350	200	15	35	35	15	19.0	40.7	18.7	21.6	20.5	35.3	24.1	20.1	FCC	FCC
20	350	200	15	35	15	35	14.0	33.2	10.5	42.3	19.2	31.3	11.1	38.4	FCC	FCC
21	350	200	15	15	35	35	12.9	16.8	26.2	44.1	24.5	13.8	23.5	38.2	FCC	FCC
22	350	200	18	27	27	27	20.1	27.7	19.4	32.7	23.0	26.0	19.1	32.0	FCC	FCC
23	350	500	27	18	27	27	26.3	19.2	23.5	30.9	32.7	15.3	19.7	32.3	FCC+BCC	FCC+BCC
24	350	500	27	27	18	27	28.5	27.7	12.1	31.7	25.4	29.0	15.6	29.9	FCC	FCC+BCC
25	350	200	27	27	27	18	31.9	26.8	18.6	22.7	30.5	56.9	22.1	20.5	FCC+BCC	FCC+BCC

#### Acknowledgment

This research is being performed using funding received from the DOE Office of Nuclear Energy's Nuclear Energy University Program (DE-NE0008678). This research was funded in part by a fellowship program sponsored by the Nuclear Regulatory Commission (NRC). Additive manufacturing work using the LENS MR-7 was made possible through funding from the Grainger Institute for Engineering and NSF DMREF award #1728933. The authors gratefully acknowledge use of facilities and instrumentation at the UW-Madison Wisconsin Centers for Nanoscale Technology (wcnt.wisc.edu) partially supported by the NSF through the University of Wisconsin-Madison Materials Research Science and Engineering Center (DMR-1720415).

Additionally, the authors would like to thank Prof. John Perepezko and his laboratory group use of their high-vacuum furnace, as well as Kim Kriewaldt and the UW-Madison IBL staff for performing the ion irradiations and modifying the vacuum chamber to accommodate the large compositional array with support from an NEUP Infrastructure grant.

## **Appendix**

#### Table A1

#### References

- [1] G.S. Was, D. Petti, S. Ukai, S. Zinkle, Materials for future nuclear energy systems, J. Nucl. Mater. 527 (2019) 151837.
- [2] P. Hejzlar, R. Petroski, J. Cheatham, N. Touran, M. Cohen, B. Truong, R. Latta, M. Werner, T. Burke, J. Tandy, M. Garrett, B. Johnson, T. Ellis, J. Mcwhirter, A. Odedra, P. Schweiger, D. Adkisson, J. Gilleland, Terrapower, LLC Traveling Wave Reactor development program overview, Nucl. Eng. Technol. 45 (6) (2013) 731–744.
- [3] M.B. Toloczko, F.A. Garner, C.R. Eiholzer, Irradiation creep and swelling of the US fusion heats of HT9 and 9Cr-1Mo to 208 dpa at ~ 400°C, J. Nucl. Mater. 212 (1994) 604-607.
- [4] T.R. Allen, D. Kaoumi, J.P. Wharry, Z. Jiao, C. Topbasi, A. Kohnert, L. Barnard, A. Certain, K.G. Field, G.S. Was, D.L. Morgan, A.T. Motta, B.D. Wirth, Y. Yang, Characterization of microstructure and property evolution in advanced cladding and duct: materials exposed to high dose and elevated temperature, Mater. Res. 30 (09) (2015) 1246-1274.
- [5] C. Lu, L. Niu, N. Chen, K. Jin, T. Yang, P. Xiu, Y. Zhang, F. Gao, H. Bei, S. Shi, M.-R. He, I.M. Robertson, W.J. Weber, L. Wang, Enhancing radiation tolerance by controlling defect mobility and migration pathways in multicomponent single-phase alloys, Nat. Commun. 7 (2016) 13564.
- [6] K. Jin, C. Lu, L.M. Wang, J. Qu, W.J. Weber, Y. Zhang, H. Bei, Effects of compositional complexity on the ion-irradiation induced swelling and hardening in Ni-containing equiatomic alloys, Scr. Mater. 119 (2016).
- [7] S.Q. Xia, Z. Wang, T.F. Yang, Y. Zhang, Irradiation behavior in high entropy alloys, J. Iron Steel Res. 22 (10) (2015) 879-884.
- [8] S.Q. Xia, X. Yang, T.F. Yang, S. Liu, Y. Zhang, Irradiation resistance in AlxCoCr-FeNi high entropy alloys, JOM 67 (10) (2015) 2340–2344.
- [9] J.W. Yeh, S.K. Chen, S.J. Lin, J.Y. Gan, T.S. Chin, T.T. Shun, C.H. Tsau, S.Y. Chang, Nanostructured high-entropy alloys with multiple principal elements: novel alloy design concepts and outcomes, Adv. Eng. Mater. 6 (5) (2004) 299-303.
- [10] D.B. Miracle, O.N. Senkov, A critical review of high entropy alloys and related concepts, Acta Mater. 122 (2017) 448-511.
- [11] Z. Wu, H. Bei, G.M. Pharr, E.P. George, Temperature dependence of the mechanical properties of equiatomic solid solution alloys with face-centered cubic crystal structures, Acta Mater. 81 (2014) 428-441.
- [12] A. Ludwig, Discovery of new materials using combinatorial synthesis and high--throughput characterization of thin-film materials libraries combined with computational methods, npj Comput. Mater. 5 (1) (2019) 70.
- T. Gebhardt, D. Music, T. Takahashi, J.M. Schneider, Combinatorial thin film materials science: from alloy discovery and optimization to alloy design, Thin Solid Films 520 (17) (2012) 5491-5499.

- [14] R. Löbel, S. Thienhaus, A. Savan, A. Ludwig, Combinatorial fabrication and highthroughput characterization of a Ti-Ni-Cu shape memory thin film composition spread, Mater. Sci. Eng. 481-482 (2008) 151-155.
- [15] P. Wilson, R. Field, M. Kaufman, The use of diffusion multiples to examine the compositional dependence of phase stability and hardness of the Co-Cr-Fe-Mn-Ni high entropy alloy system, Intermetallics 75 (2016) 15–24.

  [16] J.C. Zhao, X. Zheng, D.G. Cahill, High-throughput diffusion multiples, Mater. To-
- day 8 (10) (2005) 28-37.
- T. Borkar, B. Gwalani, D. Choudhuri, C.V. Mikler, C.J. Yannetta, X. Chen, R.V. Ramanujan, M.J. Styles, M.A. Gibson, R. Banerjee, A combinatorial assessment of AlxCrCuFeNi<sub>2</sub> (0 < x < 1.5) complex concentrated alloys: microstructure, microhardness, and magnetic properties, Acta Mater. 116 (2016) 63-76.
- [18] D.C. Hofmann, J. Kolodziejska, S. Roberts, R. Otis, R.P. Dillon, J.-O. Suh, Z.-K. Liu, J.-P. Borgonia, Compositionally graded metals: a new frontier of additive manufacturing, J. Mater. Res. 29 (17) (2014) 1899–1910.
- [19] P. Tsai, K.M. Flores, High-throughput discovery and characterization of multicomponent bulk metallic glass alloys, Acta Mater. 120 (2016) 426-434.
- [20] M. Moorehead, K. Bertsch, M. Niezgoda, C. Parkin, M. Elbakhshwan, K. Sridharan, C. Zhang, D. Thoma, A. Couet, High-throughput synthesis of Mo-Nb-Ta-W high-entropy alloys via additive manufacturing, Mater. Des. 187 (2020) 108358. [21] C. Parkin, M. Moorehead, M. Elbakhshwan, J. Hu, W.-Y. Chen, M. Li, L. He,
- K. Sridharan, A. Couet, In situ microstructural evolution in face-centered and body-centered cubic complex concentrated solid-solution alloys under heavy ion irradiation, Acta Mater. 198 (2020) 85-99.
- [22] C. Li, X. Hu, T. Yang, K.K. N.A.P., B.D. Wirth, S.J. Zinkle, Neutron irradiation response of a Co-free high entropy alloy, J. Nucl. Mater. 527 (2019) 151838.
- [23] C. Schneider-Maunoury, L. Weiss, P. Acquier, D. Boisselier, P. Laheurte, Functionally graded Ti6Al4V-Mo alloy manufactured with DED-CLAD® process, Addit. Manuf. 17 (2017) 55-66.
- [24] H. Dobbelstein, E.L. Gurevich, E.P. George, A. Ostendorf, G. Laplanche, Laser metal deposition of compositionally graded TiZrNbTa refractory high-entropy alloys using elemental powder blends, Addit. Manuf. 25 (2019) 252-262.
- K.M. Bertsch, G. Meric de Bellefon, B. Kuehl, D.J. Thoma, Origin of dislocation structures in an additively manufactured austenitic stainless steel 316L, Acta Mater. 199 (2020) 19-33.
- [26] N.A. Gokcen, The Mn-Ni (manganese-nickel) system, J. Phase Equilib. 12 (3) (1991) 313-321.
- [27] ASTM E521-96, Standard Practice for Neutron Radiation Damage Simulation by Charged-Particle Irradiation, ASTM International, West Conshohocken, PA, 1996 (Reapproved 2009).
- R.E. Stoller, M. Toloczko, G.S. Was, A.G. Certain, S. Dwaraknath, F. Garner, On the use of SRIM for Computing Radiation Damage Exposure Nuclear Instruments and Methods in Physics Research Section B: Beam Interactions with Materials and Atoms 310 75-80, 2013.
- [29] C. Zhang, M.C. Gao, CALPHAD modeling of high-entropy alloys, in: M.C. Gao, J.-W. Yeh, P.K. Liaw, Y. Zhang (Eds.), High-Entropy Alloys: Fundamentals and Applications, Springer International Publishing, Cham, 2016, pp. 399-444.
- [30] S. Gorsse, O.N. Senkov, About the reliability of CALPHAD predictions in multicomponent systems, Entropy 20 (899) (2018).
- [31] X. Xiao, L. Yu, Nano-indentation of ion-irradiated nuclear structural materials: a review, Nucl. Mater. Energy 22 (2020) 100721.
- [32] R.E. Honig, Vapor-pressure data for the solid and liquid elements, RCA Rev. 23 4) (1962) 567.
- [33] M. Li, K.M. Flores, Laser processing as a high-throughput method to investigate microstructure-processing-property relationships in multiprincipal element alloys, J. Alloys Compd. 825 (2020) 154025.
- [34] L. Shao, J. Gigax, H. Kim, F.A. Garner, J. Wang, M.B. Toloczko, Carbon contamination, its consequences and its mitigation in ion-simulation of neutron-induced swelling of structural metals, in: J.H. Jackson, D. Paraventi, M. Wright (Eds.), Proceedings of the 18th International Conference on Environmental Degradation of Materials in Nuclear Power Systems-Water Reactors, Cham, Springer International Publishing, 2019, pp. 681-693.
- [35] S.J. Zinkle, 1.03- radiation-induced effects on microstructure, Compr. Nucl. Mater. 1 (2012) 66-93.
- [36] A.F. Smith, R. Hales, Diffusion of manganese in type 316 austenitic stainless steel, Metal Sci. 9 (1) (1975) 181-184.
- [37] N. Sanaei, A. Fatemi, Defects in additive manufactured metals and their effect on fatigue performance: a state-of-the-art review, Prog. Mater Sci. (2020) 100724 In press.
- [38] S. Tammas-Williams, P.J. Withers, I. Todd, P.B. Prangnell, Porosity regrowth during heat treatment of hot isostatically pressed additively manufactured titanium components, Scr. Mater. 122 (2016) 72-76.
- [39] B.N. Singh, S.J. Zinkle, Defect accumulation in pure FCC metals in the transient regime: a review, J. Nucl. Mater. 206 (2) (1993) 212-229.